Image to Patterning: Density-specified Patterning of Micro-structured Surfaces with a Mobile Robot

Annalisa T. Taylor, Malachi Landis, Yaoke Wang, Todd D. Murphey, Ping Guo

Abstract—Micro-structured surfaces possess useful properties such as friction modification, anti-fouling, and hydrophobicity. However, manufacturing these surfaces in an affordable, scalable, and efficient manner remains challenging. Standard coverage methods for surface patterning require precise placement of micro-scale features over meter-scale surfaces with expensive tooling for support. In this work, we address the scalability challenge in surface patterning by designing a mobile robot with a credit-card-sized footprint to generate microscale divots using a modulated tool tip. We provide a control architecture with a target feature density to specify surface coverage, eliminating the dependence on individual indentation locations. Our robot produces high-fidelity surface patterns and achieves automatic coverage of a surface from sophisticated target images. We validate an exemplary application of such micro-structured surfaces by controlling the friction coefficients at different locations according to the density of indentations. These results show the potential for compact robots to perform scalable manufacturing of functional surfaces, switching the focus from precision machines to small-footprint devices tasked with matching only the density of features.

I. INTRODUCTION

Micro-structured surfaces enable a diverse set of functional properties such as friction modification [1], anti-fouling [2], anti-bacteria [3], hydrophobicity [4], anti-icing [5] and structural coloration [6]. In particular, micro-indentation, applying divots to a smooth surface, can improve hydrodynamic lubrication and trap pockets of lubricant in sliding surfaces [7]. When applied to the bodies of cars or wings of airplanes, micro-structured surfaces may vastly improve fuel economy, as micro-scale dimples have been shown to reduce friction by as much as 80% compared to smooth surfaces [8]. This presents a huge opportunity to drastically curtail fossil fuel emissions with passive material properties.

Despite the clear benefits of micro-structured surfaces, it is not yet possible to manufacture large workpieces at scale. No manufacturing techniques exist that are both low-cost and time efficient [9]. Currently, patterning large-scale workpieces would require expensive support fixtures and precision machinery, making many manufacturing techniques too cumbersome and costly for practical implementation [10]. In addition, the standard method of moving across a surface for coverage is raster scanning, a lawnmower style motion that achieves exhaustive coverage. This method consists of placing micro-scale features over meter-scale parts in a regularly spaced array [11]. Not only does raster scanning require slow and deliberate motion, it also adds design parameters

Mechanical Engineering Department, Northwestern University Corresponding authors: Ping Guo ping.guo@northwestern.edu and Todd Murphey t-murphey@northwestern.edu

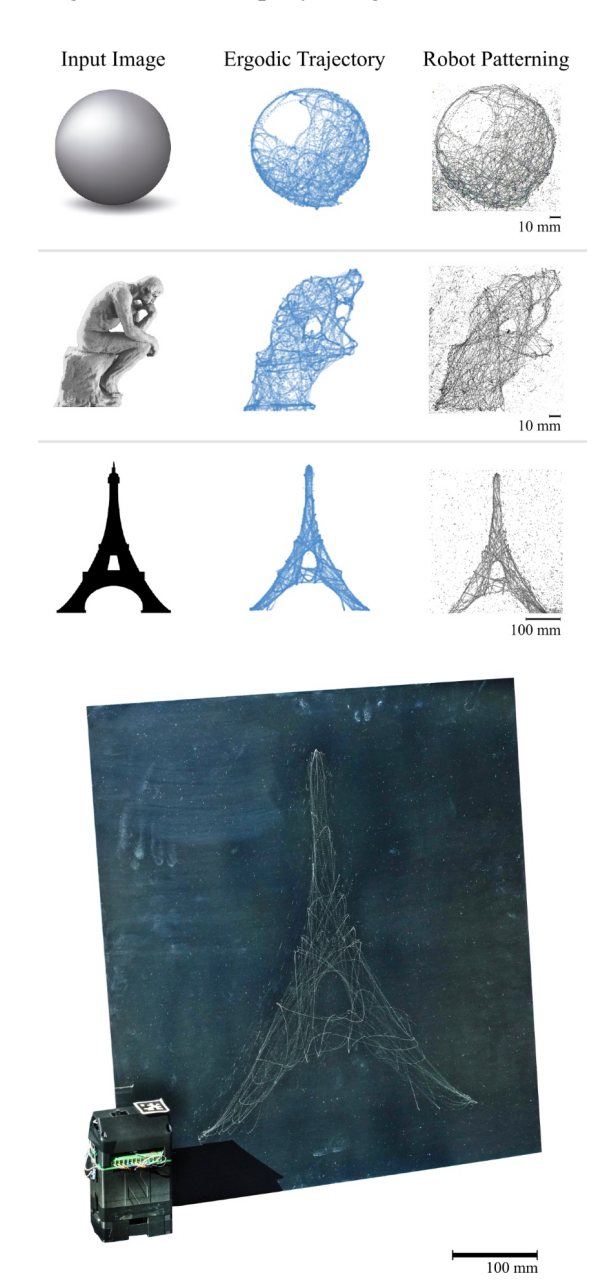


Fig. 1. From image to patterned surface. (upper) Each row shows the input image (feature density specification), the simulated ergodic trajectory, and the robot patterning on metal. The image contrast in the right column was increased between the metallic background and dimples for clarity. The background noise in these images is from scratches and dust on the metallic surface, made more visible due to the increased contrast. (lower) The robot with a patterned image of the Eiffel Tower, approximately 450 mm tall, on a polished aluminum substrate. With a footprint the size of a credit card, the robot patterned an area $35\times$ its size, demonstrating scalability.



Fig. 2. **Mobile robot patterning.** (left) The robot drives atop a workpiece, applying micro-scale indentations along its trajectory. (right) The texturing robot with an I.D. card for scale. An AprilTag on top of the robot is used for position tracking.

to translate desired high-level patterns to layouts of micro-dimples. The precision required for this coverage strategy does not necessarily result in better surface functionality as physical properties of micro-structured surfaces are often evaluated according to *densities* of features as opposed to individual placement [12]–[14]. Moreover, it has been shown that properties, such as ice adhesion and friction coefficient, can be controlled through varying the density of surface micro-structures [15]–[17], meaning that feature density can be used as a patterning specification instead of individual feature location. Shifting focus towards managing density has the potential to make the manufacturing process faster and more affordable by creating a method that does not require slow, precision tools.

To meet the need for affordable and efficient surface patterning techniques for large workpieces, we deploy a mobile robot with a credit-card-sized footprint to pattern microindentations according to a spatial distribution over a surface. Our coverage method allows the robot to move quickly even in areas of high density. With density specifications, imprecision in the mobile robot is acceptable, enabling a simplified design with low-cost components. Nevertheless, we show that this robot can pattern micro-scale features with a characteristic dimension below 100 µm on a relatively large surface ranging from tens of millimeters to half a meter in size on a single-charge (Figure 1).

To generate coverage trajectories, we provide an optimal control framework that uses feature density as an objective. Our coverage strategy is based on the property of ergodicity, which directs an agent to spend time in regions in proportion to a specified spatial distribution, in this case, the desired density of micro-indentations [18], [19]. By matching time spent in an area, the robot will re-visit high density regions to ensure adequate coverage and move quickly. A schematic of our approach is illustrated in Figure 2. With this method we demonstrate that our robot can reproduce detailed target images according to several complicated density objectives. We provide an exemplary application for the resulting microstructured surfaces by controlling the friction coefficients at different locations according to the density of indentation patterns. The primary contributions of this work are summarized below:

- 1) We provide a constrained optimal control framework for surface patterning that generates coverage trajectories from patterning specifications.
- We design, fabricate, and characterize a mobile robot for surface micro-patterning.
- We develop and experimentally demonstrate an image to texture generation pipeline to control the coefficient of friction of a metallic surface.

These results show the potential for mobile robots to perform scalable manufacturing of micro-structured functional surfaces, enabling large, precision machines to be replaced with small-scale, inexpensive devices.

II. ERGODIC COVERAGE ALGORITHM

When micro-patterning surfaces for applications such as de-icing or friction modification, the precise location of each micro-scale feature over a large workpiece is inconsequential compared to the density of features in a particular area [15]-[17]. This observation makes density functions ideal as coverage task specifications for surface patterning; density functions are compatible with the underlying physical processes that allow surface features to disrupt ice formation or reduce drag. In this section, we describe the ergodic optimal control algorithm as a method of covering spatial distributions, ensuring the density of features is proportional to the value of the target density function over the workpiece [18]. We balance the imprecision allowed in our coverage algorithm by employing Control Barrier Functions (CBFs) as a means of guaranteeing the safety of both the robot and the workpiece during the coverage process by constraining the robot's position [20].

A. Optimal Control with the Ergodic Metric

We assume the dynamics of the agent are in control-affine form:

$$\dot{x}(t) = f(x(t)) + g(x(t))u(t),$$

here, $f(x): \mathbb{R}^n \to \mathbb{R}^n$ and $g(x): \mathbb{R}^n \to \mathbb{R}^{n \times m}$ are vector fields the system's free dynamics and its response to control inputs respectively. To compare the statistics of the robot's trajectory and the target feature density, we represent their distance in Fourier space [21]. The Fourier coefficients for the trajectory statistics x(t) are $c_k = \frac{1}{\tau} \int_{t_i}^{t_i + \tau} \tilde{F}_k(x(t)) dt$, where $\tilde{F}_k(x(t)) = \frac{1}{N} \sum F_k(x(t))$ and $F_k(x)$ are cosine basis functions [18]. Additionally, we need a Fourier representation of the coverage task given by $\phi_k = \int_{\mathcal{T}} \phi(x) F_k(x) dx$ with density function $\phi(x)$. For this application, $\phi(x)$ is determined by the input images seen in Figure 1. As a result, we write an ergodic metric over Fourier space that compares the time-averaged trajectory c_k with the target density ϕ_k :

$$\mathcal{E}(x(t)) = \sum_{k \in n} \Lambda_k \left(c_k - \phi_k \right)^2, \tag{1}$$

where Λ_k is a normalization coefficient. To use this metric for optimal control, we calculate the adjoint variable of the

ergodic objective function as

$$\dot{\rho} = -2\frac{q}{\tau} \sum_{k \in r} \Lambda_k (c_k - \phi_k) \frac{\partial F_k(x)}{\partial x} - \frac{\partial f}{\partial x}^\top \rho.$$

Then, as shown in [22], we compute the optimal control action that minimizes the ergodic metric:

$$u(t) = -R^{-1}g(x)^T \rho(t),$$

where R represents a positive semi-definite regularization matrix on the control effort.

B. Achieving Bounded Coverage

Our density-based control strategy can provide efficient coverage generation compared to slow and precise traditional methods. However, manufacturing errors on large workpieces, such as airplane wings, are particularly costly. It is crucial that these workpieces are not compromised during the patterning process. For this reason we discuss a means of guaranteeing the safety of both the robot and the workpiece, allowing the robot to complete the patterning task autonomously. Here, we use Control Barrier Functions (CBFs), which guarantee safety by constraining a system within a "safe set" through the principle of forward invariance, ensuring any system starting from a safe set remains within that set. As defined in [20], a CBF is a continuously differentiable, class \mathcal{K}_{∞} function $\alpha(\cdot)$ function $h:A\to\mathbb{R}$, such that

$$L_f h(x) + L_g h(x) u \ge -\alpha(h(x))$$

for all $x \in A$. Candidates for CBFs include log functions and the distance between an agent and an obstacle and can be easily integrated as constraints in optimal control problems. In this work, we automatically synthesize CBFs from input images (which specify target feature density $\phi(x)$) based on the pixel value. This prevents the robot from running into obstacles or patterning areas of the workpiece that should be left unprocessed. We impose these barrier functions after the calculation of the optimal ergodic control, using an outer optimizer to minimally deviate from the calculated ergodic control and maintain safety. When, the agent is far from any unsafe areas, it continues to behave optimally ergodic.

III. MOBILE ROBOT DESIGN

Mobile robots are a promising substitute for the precision manufacturing tools used in surface patterning because they have no domain size limitations, meaning as the workpiece size grows, the machine tool does not need to scale with the workpiece [23]. We next discuss the design of the mobile robot shown in Figure 3 for surface micro-patterning. In this work, we modify surfaces by micro-indentation (plastic deformation). However, in future work the robotic platform can be extended to include deposition (additive) and micro-machining (subtractive) techniques.

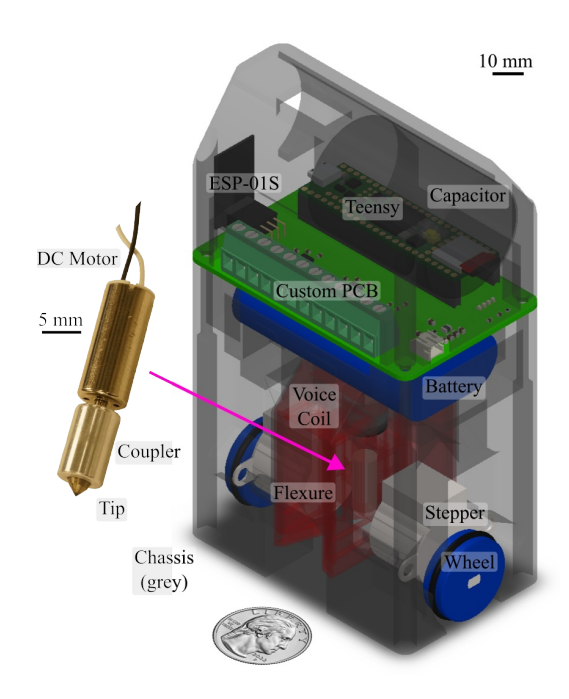


Fig. 3. **Mobile robot design.** CAD assembly of robot (right) is illustrated with the as-built indentation tool. The US quarter is placed for scale.

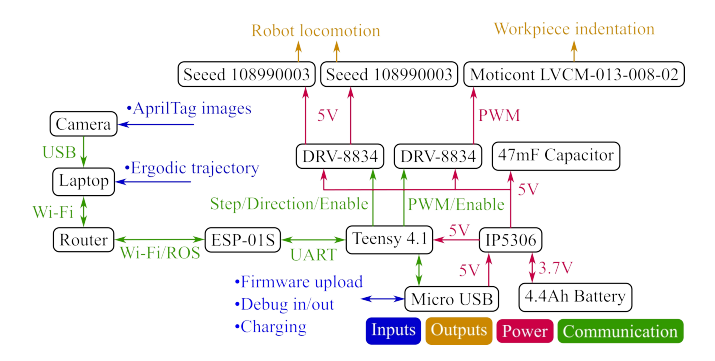


Fig. 4. **System diagram.** The robot receives external communications about its state and desired trajectory over Wi-Fi, then uses electronics integrated on a custom PCB to locomote over a workpiece and apply texturing through indentation.

A. Mobile Robot Platform

The perimeter of the robot fits within the boundaries of a credit card (85.6 mm by 54 mm) with a 3D printed chassis from the consumer-grade printer Ender 2. We use a two-wheel, differential drive configuration for simplicity, small size, and low cost. Geared stepper motors (Seeed 108990003) move the robot at a maximum linear velocity of 40 mm/s. The motion resolution is sufficient for the camera feedback to prevent drift. This imprecision inherent to the robot further demonstrates the robustness of our ergodic control strategy.

Figure 4 shows the IO, power, and communication between the robot components. We use Teensy 4.1 microcontroller with 600 MHz processor and floating point unit (FPU) to control the robot. The Wi-Fi chip (ESP-01S) provides communication with a central router for receiving commands from a laptop and transmitting status messages. The robot uses a 3.7 V, 4.4 Ah lithium-ion battery for approximately 2 hours of untethered operation. We design a custom PCB to connect all components including two motor

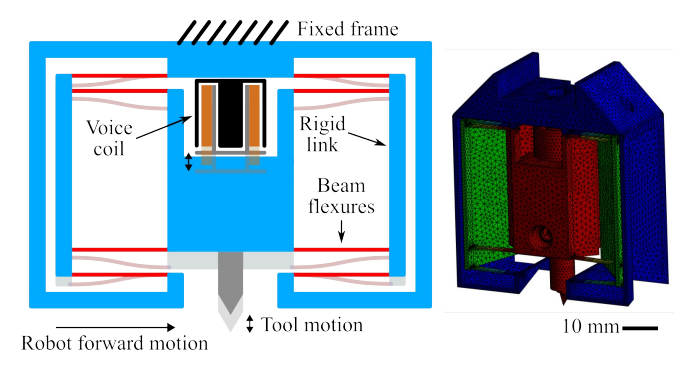


Fig. 5. **Flexure stage.** A 3D-printed flexure provides well-constrained vertical motion at low cost and complexity, shown schematically (left). Beams are 0.4 mm thick (one 3D printer nozzle-width) and printed without support to give maximum flexibility. A modal analysis (right) yields a first mode at 26 Hz.

drivers (Texas Instruments DRV-8834) and a battery charging circuit (Injoinic Technology IP5306). Pulse width modulation from the Teensy allows the voice coil power to be varied in addition to its duty cycle. A large 47 mF capacitor is wired in parallel with the power supply to smooth the periodic load from the voice coil, reducing peak current draw. The stepper driver is disabled when the robot is not moving to reduce heat input into the polymer chassis and wheels.

B. Micro-indentation Tool

We use a voice coil (Moticont LVCM-013-008-02) to drive the micro-indention tool in the axial direction where it is supported using a 3D printed, linear translation flexure mechanism, shown schematically in Figure 5. The design is based on a folded beam suspension to obtain relatively longrange linear motion [24]. Finite element analysis confirms that the designed mechanism gives high compliance (2.62 mm/N) in the axial direction and low compliance (0.09 mm/N) along the robot's direction of travel. High compliance in the axial direction allows the voice coil to efficiently drive the tool downward, while low compliance in other directions ensures the tool stays in place during operation.

The tool assembly consists of a 50,000 RPM DC motor, aluminum coupler, and carbide engraving tool in a glued assembly. The chosen tool shape is an octagonal pyramid, which produces a roughly spherical dimple shape with characteristic width and depth of approximately 65 µm and 8.5 µm (Figure 6). We demonstrate the rate of indentation production up to 20 Hz. The first mode of vibration for the flexure occurs at 26 Hz, which sets the upper limit of the bandwidth. When the robot is moving at the maximum linear velocity of 40 mm/s along with the maximum indentation frequency, it produces one surface feature every 2 mm. Notably, this distance does not set the minimal feature separation, since the patterning is prescribed according to a density function using ergodic control. The typical coverage rate in this work is 300 mm² per hour.

C. Tool Workpiece Interaction

At the unit level, tool geometry and voice coil duty cycle can impact the shape of patterned features. We tested multiple indentation tips on an aluminum work surface, both

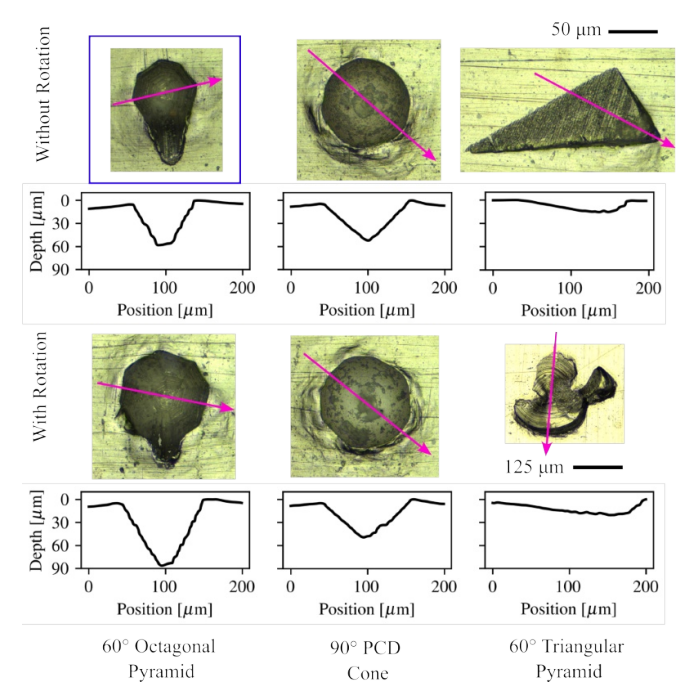


Fig. 6. The influence of tool tip geometry. Three potential tool tip designs were tested with (upper) and without (lower) rotation on an aluminum substrate. Indentations were measured and the profile was found along the line indicated by the pink arrow. The octagonal pyramid tip (blue rectangle) was selected for use throughout experiments. $50~\mu m$ scale bar applies to all images except the lower right.

with and without rotation, shown in Figure 6. The candidate tool geometry for testing includes a 90° polycrystalline diamond (PCD) cone, 60° triangular pyramid, and 60° octagonal pyramid. The triangular pyramid has a truncated tip which produced poor quality indentations. For the patterns in this work, we use the octagonal pyramid because it produces deeper indentations than the PCD cone and imprints a unique octagonal shape into the surface. As the rotary motion capability requires increased power consumption and results in a small difference in indentation shape, we forgo rotary motion in later tests. In future work, rotary motion could be used to modulate indentation geometry or machine continuous channels.

D. Software

We develop two pieces of software to integrate the ergodic control algorithm with the robotic platform. Both are available on GitHub [25]. The control computer runs a Python program to poll a camera using OpenCV and find the robot AprilTag via apriltag library [26]. ROS Melodic sends commands to the robot over Wi-Fi, batching multiple commands to accommodate the low (~5 Hz) update rate of the camera due to the demands of AprilTag identification. During batch execution, we predict the robot's position, enabling the robot's true position to update at a lower frequency than the trajectory points are executed. This is relevant to small patterns where the time steps between trajectory points are also very small, leading to a higher update rate which cannot be met by AprilTag tracking alone. The robot pauses following batch execution to prevent blurring when a new image is captured by the camera. Alternative methods such as

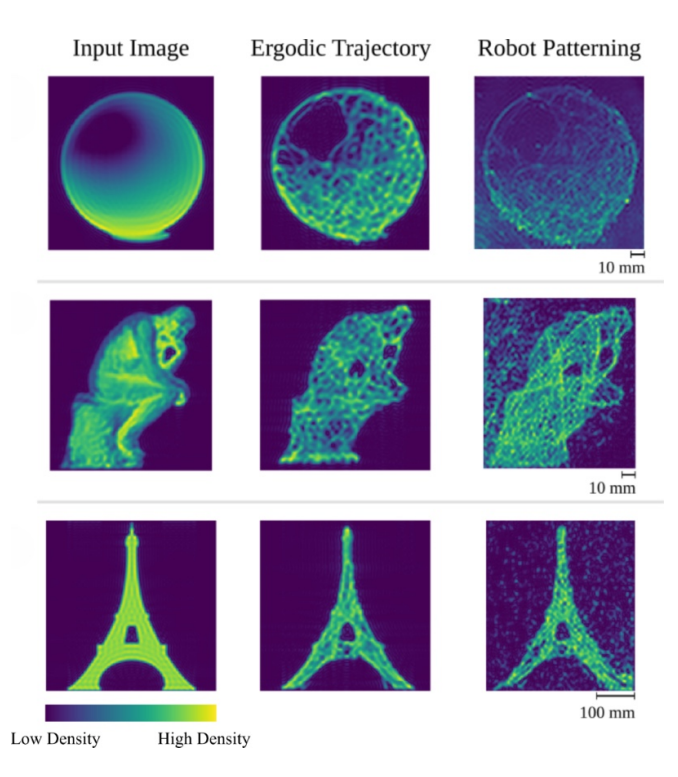


Fig. 7. Recreating input images from density specifications. Each row contains the Fourier Transform of the input image, which defines the target feature density, resulting ergodic trajectory, and photo of the patterned surface. The ergodic control algorithm optimizes the difference between the statistics of the input image to the statistics of the robot's trajectory. This comparison demonstrates the success of the algorithm in matching the robot's trajectory statistics to the input image with . For clarity, the patterned surface image has been edited to increase contrast. This brightens dust and scratches on the surface which cause the noisy background dots in the experimental images.

ultrasound beacons could be used in future work to eliminate the reliance on camera tracking.

The robot's firmware uses the Teensy Arduino libraries. The rosserial_arduino library allows ROS publishers and subscribers to run on the Teensy. WiFiEspAT handles communication over UART with the ESP-01S Wi-Fi chip, allowing wireless communication between the laptop and the robot. Timer interrupts on the Teensy manage timing for the stepper motor velocity control and tool oscillation.

IV. EXPERIMENTAL VALIDATION

A. Generated Patterns

We produce multiple patterned surfaces with different sizes and input images, including a linear gradient, an illuminated sphere, Rodin's Thinker, and the Eiffel Tower. The input images, their corresponding ergodic trajectories, and the photos of patterned surfaces are shown in Figure 1. The goal of the robot is to match its trajectory statistics, c_k , to the statistics of the input image ϕ_k (defined by $\phi(x)$) as in Equation 1. The Fourier transform of the input image, the ergodic trajectory, and the experimentally generated pattern for each are shown in Figure 7. These results validate that the micro-patterned surfaces match the target feature density.

We use an Alicona InfiniteFocus microscope to image the linear gradient surface. We measure one indentation in detail to obtain depth data as shown in Figure 8. This indentation

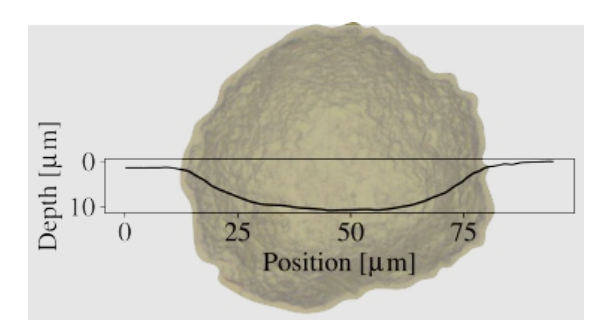


Fig. 8. **Exemplary dimple.** A dimple from the linear gradient overlaid with a plot of the depth vs. position across the dimple. The width at the surface is approximately $65 \mu m$, with a maximum depth of approximately $8.5 \mu m$.

is topologically distinct from those shown earlier, with a roughly spherical shape and no indication of the octagonal faces of the tool. This morphology can be explained by the estimated 200,000 indentations the tool tip performed before this image was captured, resulting in significant wear. Figure 9 shows the linear gradient captured with low-angle light highlighting the dimples, along with detail views which quantitatively demonstrate the change in texturing density corresponding to the change in target density.

We generate trajectories offline using a virtual agent and domain, removing any computational speed constraint from impacting the online robot control. The patterns we present here were completed with a tool oscillation frequency of 10 Hz and duty cycle of 2%. Increasing the oscillation frequency creates more closely spaced chains of dimples, while decreasing the frequency makes each dimple more distinct, with a greater effect when the time between dimples is close to the time between trajectory points. Increasing the duty cycle makes larger dimples but increases the chance of "rebound" occurring, where the tool bounces off the work surface while being forced downward by the voice coil, causing a second impact. Both of these effects may or may not be desirable depending on the surface's function.

Pattern size has the greatest impact on the time needed to pattern a given number of trajectory points. The Eiffel Tower, the largest patterning, uses 10k trajectory points over 88 minutes, while the linear gradient, the smallest patterning, uses 26.5k points and takes 55 minutes. Adding trajectory points generally increased the fidelity of the produced image. The linear gradient was completed with a 0.1 s time step, The Thinker and sphere use time steps of 0.25 s, and the Eiffel Tower used a 0.5 s time step. A sufficiently large time step ensures that enough time is allowed between trajectory points so that the wheel velocities are below their maximums.

B. Functional Surface Verification

Creating large functional surfaces composed of microscale features is a motivating application of our "image to patterning" framework. It is well-known that micro-scale surface patterns will directly affect the tribological behavior of a surface. Next, we explore the effect of indentation density on the friction coefficient of our robot patternings. We tested the linear gradient pattern shown in Figure 9

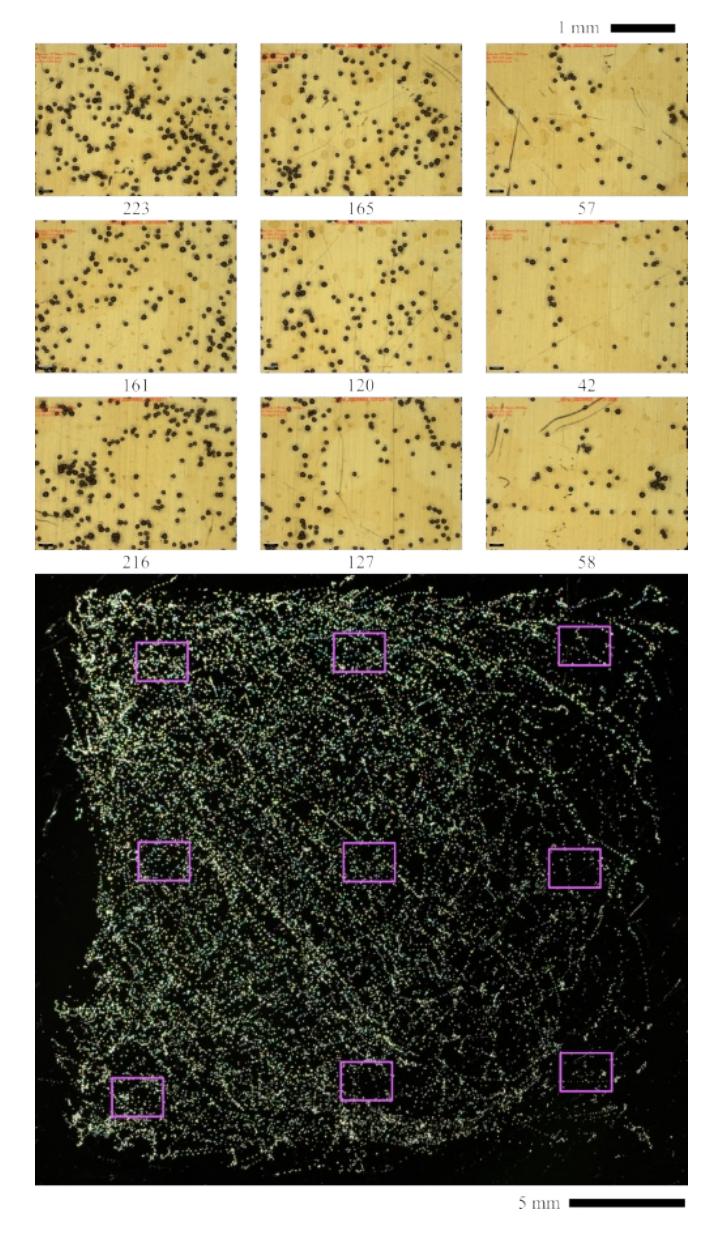


Fig. 9. **Exemplary surface patterning results.** A linear gradient (left to right, from high to low area density of dimples) patterned on polished brass by the robot. (upper) $5\times$ magnification microscope images, each covering approximately 2.85×2.15 mm, with the number of indentations within given below each image. (lower) Macro image taken with low-angle lighting to highlight indentations, with each pink rectangle corresponding to a microscope image. Qualitatively and quantitatively, the robot was able to match the target feature density.

using an Rtec MFT-5000 tribometer to determine the friction coefficient between the patterned surface and a hardened steel contact. The steel contact was formed from a 9.5 mm hardened ball bearing with a flat region approximately 7.1 mm in diameter machined by Electrical Discharge Machining (EDM). The workpiece was fully submerged in a bath of polyalphaolefin (PAO) with a viscosity of 16.8 mm²/s. We applied a normal load of 5 N and completed 30 cycles of 10 mm displacement at frequencies of 0.1, 0.5, and 2.5 Hz for each region of the pattern. The resulting friction coefficients are shown over time for each of the regions in Figure 10 along with an image of the surface after testing.

As the friction testing illustrated, the friction coefficient of the patterned surface changed depending on the density of indentations. At 0.5 Hz oscillation frequency, the friction coefficient increased monotonically with density, from 0.04 on the unpatterned surface to 0.11 at approximately 30 indentations per mm². We hypothesize the increase results from asperities raised on the periphery of individual indentations. Increasing area density results in more of these asperities in contact with the steel surface at once, thereby increasing the net friction force. This result agrees with the data captured in [11], where the friction coefficient was initially higher for the textured surface and decreased only after wear or post-texturing machining. Friction specification represents one of multiple surface property modifications that are possible with this control scheme.

V. Conclusion

In this work, we outlined a method for surface micropatterning with a mobile robot that subverts traditional manufacturing techniques by allowing a small device to pattern a large workpiece efficiently. We used an ergodic optimal control algorithm to match densities of indentations over a surface, allowing the robot to move quickly and revisit high density areas instead of deliberately texturing in precise locations. Our robot was able to recreate detailed input images by applying indentations on metallic surfaces. This was shown to modify the coefficient of friction relative to indentation density. In future work, we will run the control algorithm onboard the robot and allow the robot to localize itself. We also plan to use multiple distributed mobile robots to pattern large workpieces collectively. This work illustrates a novel manufacturing paradigm in which inexpensive, imprecise mobile robots can be used to apply functional surface micro-patterns, allowing future vehicles to improve their fuel economy, longevity, and sustainability with passive material properties.

VI. ACKNOWLEDGEMENTS

We thank Tobias Martin in Dr. Q. Jane Wang's lab for his assistance with friction testing and Allison Pinosky for helpful feedback. This research was supported by the National Science Foundation under Grant number CNS-2229170.

REFERENCES

- T. Nanbu, N. Ren, Y. Yasuda, D. Zhu, and Q. J. Wang, "Microtextures in concentrated conformal-contact lubrication: Effects of texture bottom shape and surface relative motion," *Tribology Letters*, vol. 29, pp. 241–252, 2008.
- [2] M. Salta, J. A. Wharton, P. Stoodley, S. P. Dennington, L. R. Goodes, S. Werwinski, U. Mart, R. J. Wood, and K. R. Stokes, "Designing biomimetic antifouling surfaces," *Philosophical Transactions of the Royal Society A: Mathematical, Physical and Engineering Sciences*, vol. 368, no. 1929, pp. 4729–4754, 2010.
- [3] S. T. Reddy, K. K. Chung, C. J. McDaniel, R. O. Darouiche, J. Landman, and A. B. Brennan, "Micropatterned surfaces for reducing the risk of catheter-associated urinary tract infection: An in vitro study on the effect of sharklet micropatterned surfaces to inhibit bacterial colonization and migration of uropathogenic escherichia coli," *Journal of Endourology*, vol. 25, no. 9, pp. 1547–1552, 2011.
- [4] A.-M. Kietzig, S. G. Hatzikiriakos, and P. Englezos, "Patterned superhydrophobic metallic surfaces," *Langmuir*, vol. 25, no. 8, pp. 4821–4827, 2009.

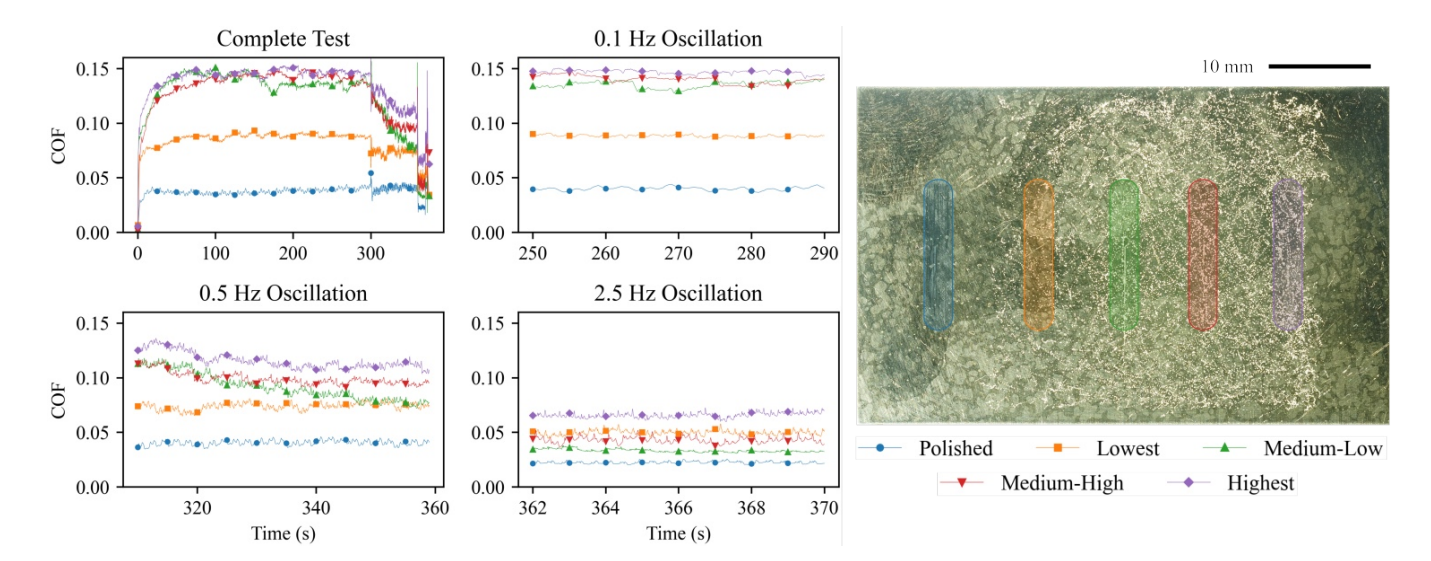


Fig. 10. Friction modification through density specification. (left) Plot of varying friction coefficients for regions of the linear gradient with different areal densities of dimples. The full data (upper left) is split into the different oscillation frequencies and re-plotted in greater detail. Lower frequency oscillations showed more monotonic behavior, with friction increasing with density. (right) The corresponding test regions. This plot shows that friction, one functional surface property out of many, can be adjusted by changing feature density.

- [5] J. Lv, Y. Song, L. Jiang, and J. Wang, "Bio-inspired strategies for anti-icing," ACS Nano, vol. 8, no. 4, pp. 3152–3169, 2014.
- [6] J. Sun, B. Bhushan, and J. Tong, "Structural coloration in nature," RSC Advances, vol. 3, no. 35, pp. 14862–14889, 2013.
- [7] A. Kovalchenko, O. Ajayi, A. Erdemir, G. Fenske, and I. Etsion, "The effect of laser surface texturing on transitions in lubrication regimes during unidirectional sliding contact," *Tribology International*, vol. 38, no. 3, pp. 219–225, 2005.
- [8] A. Ramesh, W. Akram, S. P. Mishra, A. H. Cannon, A. A. Polycarpou, and W. P. King, "Friction characteristics of microtextured surfaces under mixed and hydrodynamic lubrication," *Tribology International*, vol. 57, pp. 170–176, 2013.
- [9] B. Mei, F. Xie, X.-J. Liu, Z. Xie, and H. Zhao, "A mobile hybrid robot and its accuracy issue in machining of large-scale structures," *IEEE/ASME Transactions on Mechatronics*, pp. 1–11, 2023.
- [10] D. Patel, V. Jain, and J. Ramkumar, "Micro texturing on metallic surfaces: State of the art," *Proceedings of the Institution of Mechanical Engineers, Part B: Journal of Engineering Manufacture*, vol. 232, no. 6, pp. 941–964, 2018.
- [11] J. Shimizu, T. Nakayama, K. Watanabe, T. Yamamoto, T. Onuki, H. Ojima, and L. Zhou, "Friction characteristics of mechanically microtextured metal surface in dry sliding," *Tribology International*, vol. 149, p. 105634, 2020, 45th Leeds-Lyon Symposium on Tribology "Smart Tribology Systems".
- [12] Q. Sun, T. Hu, H. Fan, Y. Zhang, and L. Hu, "Dry sliding wear behavior of tc11 alloy at 500 c: Influence of laser surface texturing," *Tribology International*, vol. 92, pp. 136–145, 2015.
- [13] C. Gachot, A. Rosenkranz, S. Hsu, and H. Costa, "A critical assessment of surface texturing for friction and wear improvement," *Wear*, vol. 372, pp. 21–41, 2017.
- [14] M. Vishnoi, P. Kumar, and Q. Murtaza, "Surface texturing techniques to enhance tribological performance: A review," *Surfaces and Interfaces*, vol. 27, p. 101463, 2021.
- [15] L. Vilhena, M. Sedlaček, B. Podgornik, J. Vižintin, A. Babnik, and J. Možina, "Surface texturing by pulsed nd: Yag laser," *Tribology*

- International, vol. 42, no. 10, pp. 1496-1504, 2009.
- [16] L. Dan, Y. Xuefeng, L. Chongyang, C. Jian, W. Shouren, and W. Yanjun, "Tribological characteristics of a cemented carbide friction surface with chevron pattern micro-texture based on different texture density," *Tribology International*, vol. 142, p. 106016, 2020.
- [17] X. Tong, J. Shen, and S. Su, "Properties of variable distribution density of micro-textures on a cemented carbide surface," *Journal of Materials Research and Technology*, vol. 15, pp. 1547–1561, 2021.
- [18] L. M. Miller, Y. Silverman, M. A. MacIver, and T. D. Murphey, "Ergodic exploration of distributed information," *IEEE Transactions on Robotics*, vol. 32, no. 1, pp. 36–52, 2016.
- [19] A. T. Taylor, T. A. Berrueta, and T. D. Murphey, "Active learning in robotics: A review of control principles," *Mechatronics*, vol. 77, p. 102576, 2021.
- [20] A. D. Ames, S. Coogan, M. Egerstedt, G. Notomista, K. Sreenath, and P. Tabuada, "Control barrier functions: Theory and applications," in *European Control Conference (ECC)*, 2019, pp. 3420–3431.
- [21] G. Mathew and I. Mezić, "Metrics for ergodicity and design of ergodic dynamics for multi-agent systems," *Physica D: Nonlinear Phenomena*, vol. 240, no. 4-5, pp. 432–442, 2011.
- [22] A. Mavrommati, E. Tzorakoleftherakis, I. Abraham, and T. D. Murphey, "Real-time area coverage and target localization using receding-horizon ergodic exploration," *IEEE Transactions on Robotics*, vol. 34, no. 1, pp. 62–80, 2018.
- [23] X. Zhao, H. Lu, W. Yu, B. Tao, and H. Ding, "Vision-based mobile robotic grinding for large-scale workpiece and its accuracy analysis," *IEEE/ASME Transactions on Mechatronics*, vol. 28, no. 2, pp. 895– 906, 2023.
- [24] L. L. Howell, "Compliant mechanisms," in 21st Century Kinematics: The 2012 NSF Workshop. Springer, 2013, pp. 189–216.
- [25] A. T. Taylor and M. Landis, "Arduino-etching," https://github.com/ atulletaylor/Arduino-Etching, 2023.
- [26] E. Olson, "AprilTag: A robust and flexible visual fiducial system," in IEEE International Conference on Robotics and Automation, 2011, pp. 3400–3407.